

# Erosive Aggressiveness of Collapsing Cavitating Structures

<sup>1</sup>Sören Schenke\*; <sup>1,2</sup>Tom J.C. van Terwisga

<sup>1</sup>Delft University of Technology, Delft, the Netherlands; <sup>2</sup>Maritime Research Institute Netherlands, Wageningen, the Netherlands

## Abstract

The erosive aggressiveness of idealized cavities collapsing on a flat surface is investigated by numerical simulation, employing the cavitation intensity approach by Leclercq et al (2017) as a measure of the local energy impact rate. We propose a more straight forward formulation of the cavitation intensity model and verify that it satisfies energy conservation requirements for the accumulated surface energy. Based on the cavitation intensity model, statistical aggressiveness indicators are proposed. The indicators account for the rapidness and frequency of the collapse events. The aggressiveness indicators are further applied to a NACA0015 hydrofoil surface.

**Keywords:** cavitation erosion, impact energy, aggressiveness indicator, pressure recovery

## Introduction

From an energy point of view, the erosive aggressiveness of a cavity imploding close to a solid surface depends for one part on its ability to focus its impact energy on the surface. The surface distribution of impact energy accumulating throughout a collapse event partially depends on the cavity shape and its orientation relative to the surface. Starting from the potential energy approach by Vogel and Lauterborn (1988), Leclercq et al (2017) have proposed a cavitation intensity model for the instantaneous energy impact rate on a solid surface caused by collapsing cavities. The cavitation intensity model is derived from the solid angle projection of the released power on discrete triangular elements of the impacted surface. We propose a more straight forward and fully continuous form of the cavitation intensity model. This facilitates its application and allows to make analytical predictions on the amount of accumulated surface energy in certain situations, which are employed for numerical validation in this study. The erosive aggressiveness is further thought to depend on the rapidness of the collapse event and, in periodic flow, the impact frequency. Based on the cavitation intensity model, aggressiveness indicators are proposed that account for both effects. A distinct weak point of this modelling approach is that it involves the knowledge of the ambient pressure driving the cavity collapse, which is typically unknown in more complex flow situations. A solution to this problem is suggested by Arabnejad and Bensow (2017), who trace the cavity collapses individually to reconstruct the driving ambient pressure from a set of kinematic parameters employing the Rayleigh-Plesset equation. However, this approach requires any cavitating structure to be simplified to a spherical bubble of equivalent volume. Since we deliberately address the effect of cavity shape and surface orientation, we assume that the driving pressure field of a periodic cavitating flow can be approximated by the time averaged pressure field, thereby accounting for the effect of spatial pressure recovery on statistical average. The effect of pressure recovery and the feasibility of the aggressiveness indicators is demonstrated for the cavitating flow around a NACA0015 hydrofoil.

## Erosion Intensity Model

Following Vogel and Lauterborn (1988), the potential energy of a cavity with volume  $V$  and liquid volume fraction  $\gamma = (\rho - \rho_v)/(\rho_l - \rho_v)$  is given by  $E_{pot} = (1 - \gamma)(p_\infty - p_v)V$ , where  $p_v$  denotes the vapor pressure and  $p_\infty$  the ambient pressure driving the cavity collapse. As the cavity collapses, the instantaneous rate of energy release is given by  $\partial E_{pot}/\partial t$ . Due to the linearity of these expressions, the energy release rate of the entire cavity is equal to the volume integral of the differential point source release rate  $\partial e_{pot}/\partial t$ . As indicated by Figure 1, this allows to reconstruct both the local surface impact rate  $\partial e_s/\partial t$  as well as the overall surface integrated impact rate  $\partial E_s/\partial t$  from either the local change of volume fraction  $\gamma$  or the volume change of the entire cavity, resulting in the notations

$$\left. \frac{\partial e_s}{\partial t} \right|_{\dot{\gamma}} = -X \frac{\partial e_{pot}}{\partial t}, \quad \left. \frac{\partial E_s}{\partial t} \right|_{\dot{\gamma}} = \int_{surf} \left. \frac{\partial e_s}{\partial t} \right|_{\dot{\gamma}} dS, \quad \left. \frac{\partial e_s}{\partial t} \right|_{\dot{V}} = - \int_{vol} X \frac{\partial e_{pot}}{\partial t} dV \quad \text{and} \quad \left. \frac{\partial E_s}{\partial t} \right|_{\dot{V}} = \int_{surf} \left. \frac{\partial e_s}{\partial t} \right|_{\dot{V}} dS, \quad (1)$$

where  $X$  is the projection operator that converts locally released power to local surface impact power, depending on the distance from the emission source and the surface orientation relative to the source. Flageul et al (2012) determine

the local potential energy release  $\partial e_{pot}/\partial t$  from the Lagrangian time derivative of mixture density. Alternatively, the energy release can be calculated from the Lagrangian time derivative of liquid volume fraction, which gives

$$\frac{\partial e_{pot}}{\partial t} = -\left(\frac{\partial \gamma}{\partial t}\right)_{div}^+ (p_\infty - p_v), \quad \text{where} \quad \left(\frac{\partial \gamma}{\partial t}\right)_{div}^+ = \max\left[-\nabla \cdot u \left(\gamma + \frac{\rho_v}{\rho_l - \rho_v}\right), 0\right]. \quad (2)$$

The ‘+’ index indicates that only condensation is taken into account. Assuming that each point source emits its potential energy as a radial wave of infinitely large propagation speed, Leclercq et al (2017) define the potential power impact per discrete surface element  $\Delta S$  from the solid angle projection of the radial source on a planar triangle as presented in the work by Van Oosterom and Strackee (1983). A continuous form of the energy impact rate on a surface location with local normal vector  $\vec{n}$  is derived by employing the projection operator

$$X = \frac{1}{4\pi} \left( \frac{\vec{x} \cdot \vec{n}}{|\vec{x}|^3} \right), \quad (3)$$

where  $\vec{x}$  denotes the vector from the impacted surface location to the center of the emission source as shown in Figure 1. Integration of the bracket term in Equation (3) over an arbitrary convex surface gives the solid angle  $\Omega$  as used in the work by Leclercq et al (2017). From the continuous form of the cavitation intensity model, it can be shown analytically that the integrated impact rate is equal to the emission rate of a volume source on any closed convex surface around the source. It is equal to half of the emission rate on a flat surface stretched to infinity, hence

$$\oint_{convex\ surface} \frac{\partial e_S}{\partial t} \Big|_{\vec{v}} dS = \frac{\partial E_{pot}}{\partial t} \quad \text{and} \quad \int_{plain\ surface} \frac{\partial e_S}{\partial t} \Big|_{\vec{v}} dS = \frac{1}{2} \frac{\partial E_{pot}}{\partial t}. \quad (4)$$

For simplicity,  $\dot{e}_S$  and  $\dot{E}_S$  are further on referred to as the local and the surface integrated impact rate caused by volume sources. A statistical measure for the aggressiveness distribution is given by the aggressiveness indicators

$$\langle \dot{e}_S \rangle_{e_S} = \frac{1}{e_S} \int_0^{e_S} \dot{e}_S de_S \quad \text{and} \quad \langle \dot{e}_S \rangle_f = \left( \frac{1}{T} \int_0^{e_S} \dot{e}_S de_S \right)^{1/2}, \quad \text{where} \quad e_S(t) = \int_0^t \dot{e}_S(t) dt. \quad (5)$$

The indicator  $\langle \dot{e}_S \rangle_{e_S}$ , being the local energy impact rate  $\dot{e}_S(t)$  averaged over the accumulated energy  $e_S$ , has a tendency to amplify local extreme events, because for the same amount of accumulated energy, it is proportional to the rate at which the surface is impacted. In case of a periodic impact signal with uniform amplitude, it is independent from the impact frequency due to the normalization by the accumulated energy, whereas the indicator  $\langle \dot{e}_S \rangle_f$  is also proportional to the impact frequency. Normalization by the sample time  $T$  causes it to converge as  $T \rightarrow \infty$ .

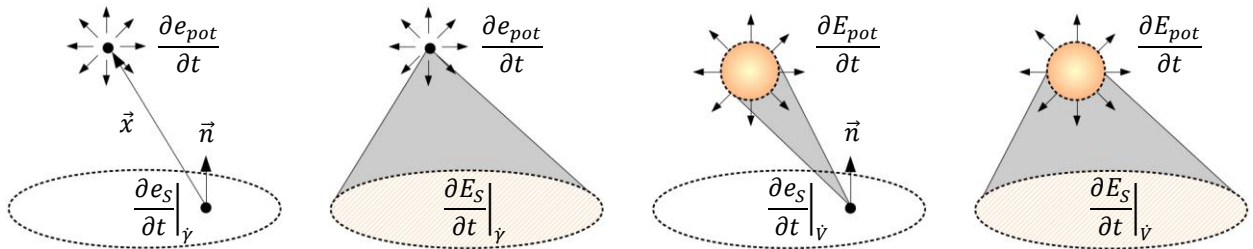


Figure 1: Terminology of energy time derivatives

## Numerical Testcases

The cavitation intensity model is implemented in the open source CFD environment OpenFOAM (2017). Viscous forces and surface tension are neglected in the momentum equation of the flow model. Phase transition is modelled by the mass transfer approach, where the model by Merkle et al (1998) is employed in a slightly modified form as presented in the work by Schenke and Van Terwisga (2017). In the pure liquid and vapor limits, the flow is assumed to be incompressible and a pressure equation is solved with subsequent momentum correction. The erosive

aggressiveness of three different cavity types is investigated. Those are, as shown in Figure 2, a horseshoe cavity, a parallel ring cavity and a bubble, all collapsing on a flat surface which is large enough to verify Equation (4). The initial bubble volume is equal to the horseshoe volume and the ring volume is twice the horseshoe/bubble volume. The torus diameter is  $R_t = 6$  mm and the tube radius  $r = 2$  mm. Both the parallel ring and the bubble are initialized at  $h = 0.5$  mm above the surface. The inner part of the computational domain is indicated in Figure 3. It consists of a cubic block structured grid of 20 mm edge length, uniformly subdivided by 55 cells in all directions. The overall volume of the domain is 32 m<sup>3</sup>. A time step size of  $\Delta t = 1.0 \cdot 10^{-7}$  s turned out to be sufficiently small to obtain a converged cavity collapse time. Additionally, a free bubble collapse is simulated and the collapse time is compared to the analytical solution of the Rayleigh-Plesset equation. As indicated in Figure 3, the solid bottom plane, treated as a slip wall, is replaced by a symmetry plane in this case. With  $C_c$  and  $C_v$  being the condensation and evaporation mass transfer coefficients of the modified Merkle model (Schenke and Van Terwisga 2017), the simulation is conducted for  $C_c = C_v = 1000$  kgs/m<sup>5</sup>, which is sufficiently large for the collapse to be inertia driven. The pressure field is initialized with  $p_v = 2340$  Pa inside the cavities and  $p_\infty = 1$  bar outside the cavities. To avoid unrealistic behavior due to the initial pressure jump across the interface, the pressure equation is solved first, thereby providing a solution of the Laplace equation as the flow is at rest initially. Figure 3 exemplarily shows the pressure field close to the beginning of the horseshoe cavity collapse. It is further noted that the reconstruction of the positive Lagrangian time derivative  $(\partial\gamma/\partial t)_{div}^+$  in Equation (2) involves numerical errors that may eventually violate the energy balance. To verify the cavitation intensity model itself, this effect is eliminated for the cavity collapse study by assuming that the change of vapor volume in the entire domain predicted from the divergence field differs from the actual vapor volume change predicted by the  $\gamma$ -time derivative by a correction factor. This factor is applied to Equation (2) at each cell individually.

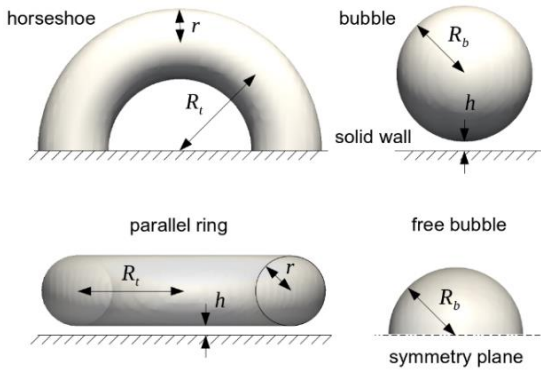


Figure 2: Idealized cavities investigated in this study

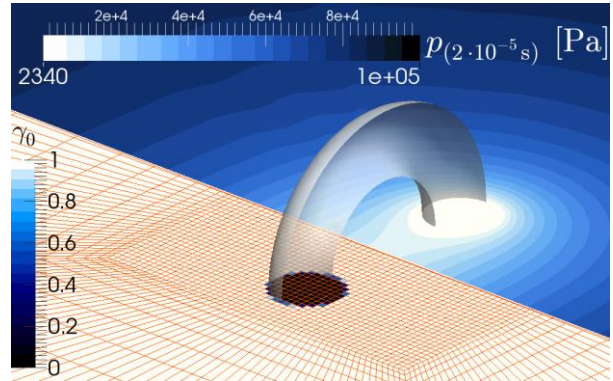


Figure 3: Initial horseshoe cavity (iso-surface for  $\gamma_0 = 0.5$ ) and bottom plane with initial  $\gamma$ -field and pressure field at  $2 \cdot 10^{-5}$  s

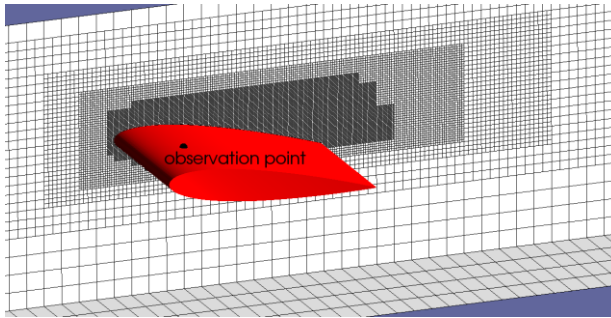


Figure 4: Grid refinement levels and observation point on the foil surface at 20% cord length

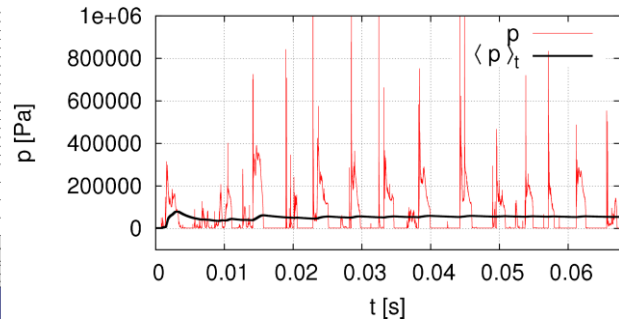


Figure 5: Pressure signal and evolution of the corresponding time averaged pressure  $\langle p \rangle_t$  at the observation point in Figure 4.

The analysis is further carried out for the cavitating flow around a NACA0015 hydrofoil in a tunnel section. The flow conditions are in line with an experiment by Van Rijsbergen et al (2012), where the angle of attack is 8° at an inflow speed of 17.3 m/s and an ambient pressure of 302295 Pa. Cordlength and span are 6 cm and 4 cm, respectively. The grid, as shown in Figure 4, corresponds to what is referred to as the fine grid in previous work by Schenke and Van Terwisga (2017), where further details on grid properties and solver settings are found. The simulation is conducted

for  $C_c/C_v = 2$ ,  $C_c = 5000$  kgs/m<sup>5</sup> and  $\Delta t = 7.5e-07$  s. For these settings, a converged pressure impact frequency of 193 Hz has been found by FFT analysis, being in good agreement with the shedding frequency of 188 Hz found by Van Rijsbergen et al (2012) in their experiment. In addition to the previous work, the time averaged pressure field  $\langle p \rangle_t$  under cavitating flow conditions is computed. We assume the time averaged pressure field to be the steady field driving the cavity collapses such that  $\langle p \rangle_t$  locally represents the driving pressure  $p_\infty$  in Equation (2). Figure 5 exemplarily depicts the pressure signal and the evolution of the corresponding time averaged pressure at an observation on the foil surface at mid-span and 20% cord length (see Figure 4).

## Results & Discussion

Figure 6 depicts the evolution of vapor volume  $V_v$  and accumulated surface energy  $E_S$  over time for the cavities shown in Figure 2. Towards the end of the collapse, the accumulated surface energy  $E_S$  converges to 50% of the initial potential energy  $E_{pot}$ , thereby verifying Equation (4). The analytical solution obtained from the Rayleigh-Plesset equation without viscous and surface tension forces is included as a reference solution for the free bubble collapse. Satisfactory agreement of the predicted collapse time is achieved. Since the presence of the wall weakens the lower half of the pressure field driving the close wall bubble collapse, the free bubble collapses faster. For the same reason the horseshoe cavity collapses faster than the parallel ring because it is not as strongly subjected to wall interaction.

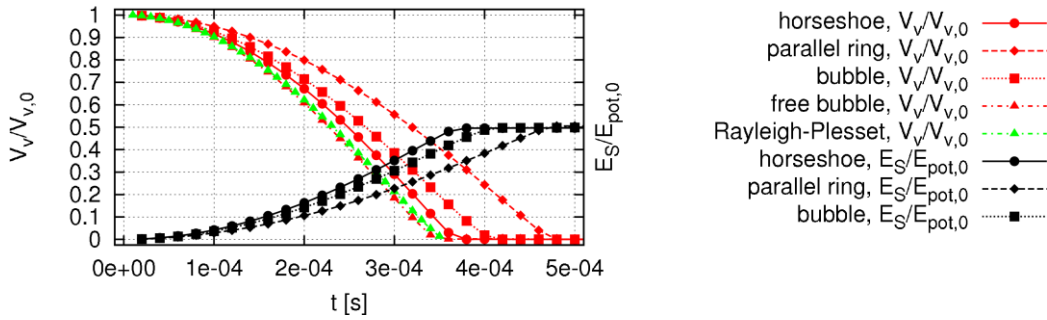


Figure 6: Evolution of vapor volume and accumulated surface energy for the cavity types depicted in Figure 2 collapsing on a flat surface

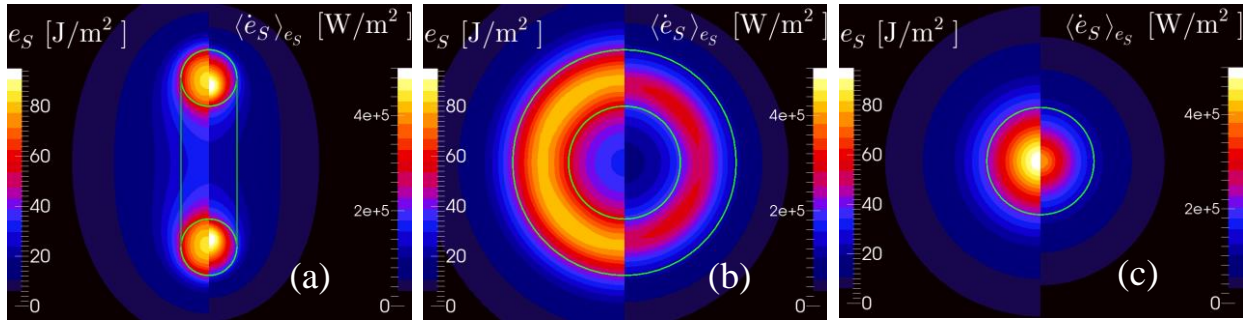


Figure 7: Accumulated surface energy  $e_s$  (left) and distribution of the aggressiveness indicator  $\langle \dot{e}_s \rangle_{e_s}$  (right) for the horseshoe cavity (a), the parallel ring cavity (b) and the spherical bubble (c) with the green line indicating the outline of the corresponding initial cavity shape

To gain more insight into the energy focusing abilities of the different cavity types, Figure 7 depicts the corresponding distributions of accumulated surface energy  $e_s$  and the distributions of the aggressiveness indicator  $\langle \dot{e}_s \rangle_{e_s}$ . In this particular case, all three cavities exhibit similar abilities to focus their potential energy towards the surface. The different collapse times, however, clearly reflect in the distributions of the aggressiveness indicator  $\langle \dot{e}_s \rangle_{e_s}$ , indicating that the horseshoe cavity is most aggressive, followed by the bubble of equivalent volume. The aggressiveness indicator  $\langle \dot{e}_s \rangle_{e_s}$  also predicts a more focused impact distribution than the accumulated surface energy  $e_s$ . It is further observed for the horseshoe and the ring cavity that especially the peak value of the indicator  $\langle \dot{e}_s \rangle_{e_s}$  exhibits a slight eccentricity from the torus center line towards the torus center, which is motivated by the circumstance that a Laplacian pressure field exhibits a larger driving force outside from the torus center line than from the inside. This is a distinct shape effect and shows that it is not entirely correct to assume the initial potential cavity energy to be proportional to the ambient pressure  $p_\infty$ . Even in the absence of wall interaction, the driving pressure may vary over the cavity surface

because, depending on its shape, the cavity also interacts with itself to some extent. The same applies to cavity-cavity interaction. This makes the determination of the driving ambient pressure  $p_\infty$  a problem of distinct difficulty.

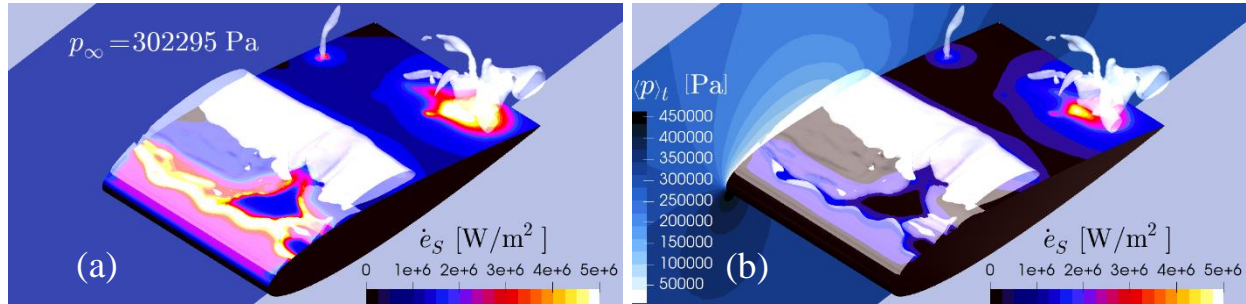


Figure 8: Instantaneous vapor structures for iso-surfaces of  $\gamma = 0.5$  and energy impact rate for uniform driving pressure  $p_\infty$  (a) and variable driving pressure  $\langle p \rangle_t$  (b)

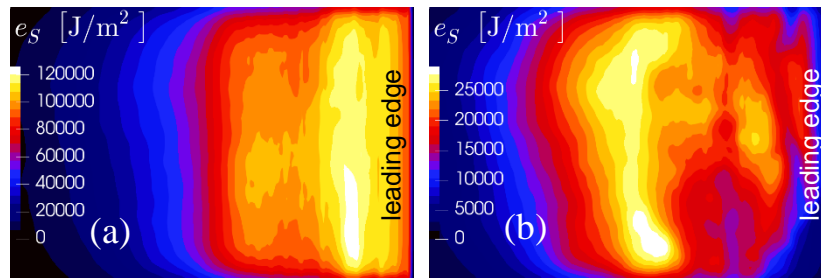


Figure 9: Accumulated surface energy on the NACA0015 hydrofoil surface for uniform  $p_\infty$  (a) and variable driving pressure  $\langle p \rangle_t$  (b) after 0.27 s

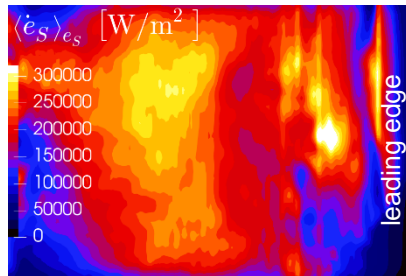


Figure 10: Distribution of the aggressiveness indicator  $\langle \dot{e}_S \rangle_{e_S}$  on the NACA0015 hydrofoil surface, accounting for pressure recovery

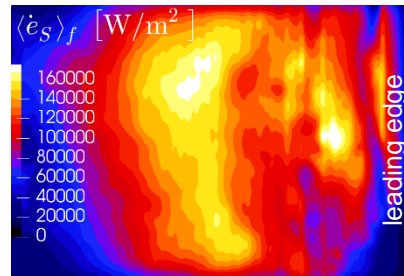


Figure 11: Distribution of the aggressiveness indicator  $\langle \dot{e}_S \rangle_f$  on the NACA0015 hydrofoil surface, accounting for pressure recovery

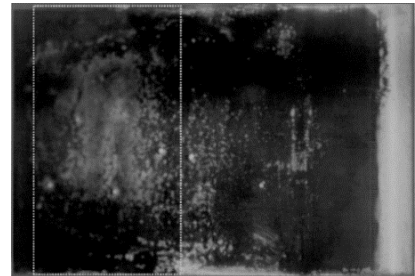


Figure 12: Damage pattern on the NACA0015 hydrofoil surface identified from paint test experiments by Van Rijsbergen et al (2012)

In case of a periodic flow, we can at least account for the effect of spatial pressure recovery on statistical average by assuming that the driving pressure field is given by the time averaged pressure field under cavitating flow conditions. Figure 8 (a) shows the distribution of the instantaneous energy impact rate  $\dot{e}_S$  for uniform driving pressure  $p_\infty$ . The same flow situation is depicted in Figure 8 (b), however with the driving pressure  $p_\infty$  being equal to the time averaged pressure  $\langle p \rangle_t$  as depicted on the tunnel side wall. This inevitably results in a larger predicted impact rates towards the leading edge, which is also clearly reflected by the distribution of accumulated surface energy  $e_S$ , shown in Figure 9 (a) for uniform driving pressure  $p_\infty$  and in Figure 9 (b) for variable driving pressure  $\langle p \rangle_t$ . The rapidness of the impacts is assessed by the aggressiveness indicators  $\langle \dot{e}_S \rangle_{e_S}$  and  $\langle \dot{e}_S \rangle_f$  given by Equation (5). Both result in similar impact distributions, indicating regions of distinct periodic impacts caused by the re-entrant jet mechanism rather than regions of scattered impacts. The indicator  $\langle \dot{e}_S \rangle_{e_S}$  further amplifies isolated events at the trailing edge because its magnitude is independent from the impact frequency. The so identified regions of high erosion risk qualitatively agree with the damage pattern obtained by Van Rijsbergen et al (2012) from experimental paint tests (Figure 12), although the main impact region identified from the simulation is somewhat closer to the leading edge and less focused towards the mid-span. The latter observation may partially be explained by the neglect of viscous forces which, if present at the tunnel wall, may cause a deflection of the re-entrant jet towards the mid-span (Dular and Petkovšek, 2015). It should further

be noted that the paint test by Van Rijsbergen et al (2012) was conducted for one hour, whereas the simulation time is only 0.27 s, not yet enough to obtain a fully converged impact distribution.

## Conclusion

A continuous form of the cavitation intensity model by Leclercq et al (2017) is presented in this study, providing a measure for the instantaneous impact power on a surface subjected to cavity collapses. The distribution of accumulated surface energy shows that the idealized horseshoe cavity, the parallel ring cavity and the bubble exhibit similar efficiencies in focusing their initial potential energy towards a confined space on the surface, given that the bubble and the parallel ring collapse very close to the surface. More pronounced differences have been found regarding the rapidness of the collapse event, which is strongly affected by the cavity shape and wall interaction effects. An aggressiveness indicator derived from the cavitation intensity approach indicates that the horseshoe cavity is more aggressive than a bubble of equivalent volume, which again turns out to be more aggressive than a parallel ring cavity of same torus and tube diameter as the horseshoe. Further taking into account that the impact power of the bubble and the parallel ring decreases considerably with increasing distance from the impacted surface, leads to the conclusion that the horseshoe cavity attached to the surface is most likely to result in damaging collapse events. Next to the rapidness of the collapse event, the effect of spatial pressure recovery has been identified as a second crucial effect since it strongly affects the distribution of initial potential cavity energy eventually impacting the solid surface. On time average, the flow around the NACA0015 hydrofoil investigated in this study exhibits a pronounced pressure recovery gradient, thereby increasing the flow aggressiveness towards the trailing edge. However, the exact determination of the pressure effectively driving the individual cavity collapses remains an issue of distinct difficulty and requires further research.

## Acknowledgements

This research is funded by the CaFE ITN initiative and the MARIN academy. We thank both institutions for their collaboration and we highly appreciate the inspiring discussions on cavitation erosion mechanisms.

## References

- [1] Arabnejad, M.H. and Bensow, R. (2017). *A Methodology to Identify Erosive Collapse Events in Incompressible Simulation of Cavitating Flows*. Proceedings of the 20<sup>th</sup> Numerical Towing Tank Symposium, Wageningen, the Netherlands.
- [2] Dular, M. and Petkovšek, M. (2015). *On the Mechanisms of Cavitation Erosion – Coupling High Speed Videos to Damage Patterns*. Experimental Thermal and Fluid Science. 68(2015), pp. 359-370.
- [3] Flageul, C., Fortes-Patella, R. and Archer, A. (2012). *Cavitation Erosion Prediction by Numerical Simulations*. Proceedings of the 14<sup>th</sup> International Symposium on Transport Phenomena and Dynamics of Rotating Machinery, Honolulu, HI, USA.
- [4] Leclercq, C., Archer, A., Fortes-Patella, R. and Cerru, F. (2017). *Numerical Cavitation Intensity on a Hydrofoil for 3D Homogeneous Unsteady Viscous Flows*. International Journal of Fluid Machinery and Systems. 10(3), pp. 254-263.
- [5] Merkle, C.L., Feng, J.Z., and Buelow, P.E.O. (1998). *Computational Modelling of the Dynamics of Sheet Cavitation*. Proceedings of the 3<sup>rd</sup> International Symposium on Cavitation, Grenoble, France.
- [6] OpenFOAM (2017). OpenFOAM web site, 2017.
- [7] Schenke, S. and van Terwisga, T.J.C. (2017). *Numerical Prediction of Vortex Dynamics in Inviscid Sheet Cavitation*. Proceedings of the 20<sup>th</sup> Numerical Towing Tank Symposium, Wageningen, the Netherlands.
- [8] Van Oosterom, A. and Strackee, J. (1983). *The Solid Angle of a Plane Triangle*. IEEE transactions on Biomedical Engineering, No. 2, pp. 125–126.
- [9] Van Rijsbergen, M., Foeth, E.-J., Fitzsimmons, P. and Boorsma, A. (2012). *High-Speed Video Observations and Acoustic-Impact Measurements on a NACA 0015 Foil*. Proceedings of the 8<sup>th</sup> International Symposium on Cavitation, Singapore.
- [10] Vogel, A. and Lauterborn, W. (1988). *Acoustic Transient Generation by Laser-Produced Cavitation Bubbles near Solid Boundaries*. The Journal of the Acoustical Society of America. 84(2), pp. 719-731.